



TECHNICAL ARTICLE

# The Effect of Heat Treatments on the Properties of a Ferritic High-Chromium Cast Iron

Adnane ElJersifi , Khalil Aouadi, Meriem Ben Ali, Abdelouahed Chbihi, Nawal Semlal, Hassan Bouaouine, and Sanae Naamane

Submitted: 30 April 2022 / Revised: 8 October 2022 / Accepted: 19 November 2022 / Published online: 15 December 2022

This paper examines the impact of heat treatments on a ferritic high-chromium cast iron's properties and resistance to erosion and corrosion. For that purpose, four samples were submitted to different temperatures (800, 900, 1000 and 1100 °C) for 2 h and then air-cooled. All samples were then studied in terms of hardness, microstructure, resistance to erosion and resistance to corrosion. Results showed that heat treatments affected those properties through three mechanisms: carbide coalescence, carbide dissolution and ferrite recrystallization. In fact, carbide coalescence slightly increased carbide thickness and volume fraction which in turn improved wear resistance. At around 1000 °C, carbide dissolution replaces coalescence inducing wear resistance loss, while the resistance to corrosion improves due to the added chromium content in the matrix. At higher temperatures, ferrite recrystallization occurs, resulting in the softening of the matrix grains which lowers wear resistance. Nevertheless, the overall hardness value increases due to the smaller grain size.

**Keywords** chromium carbides, corrosion, erosion, high-chromium cast irons, recrystallization

## 1. Introduction

High-chromium cast irons (HCCIs) are among the most used material for crushing, screening and slurry pumping applications where resistances to abrasion–corrosion and to erosion–corrosion are critical (Ref 1). HCCIs are characterized by their good corrosion resistance (Ref 2), a property owed to their high chromium content. They are also known for their high wear resistance (Ref 1, 3), as a result of their dense network of hard chromium carbides (Ref 4, 5). According to the literature, these two properties can be modified through two methods: the modification of its chemical composition and the application of appropriate heat treatments.

**Adnane ElJersifi**, Mohammedia School of Engineers (EMI), Mohammed V University, Avenue Ibn Sina, B.P. 765, Agdal, Rabat, Morocco; and Mohammed ElJazouli, Rabat Design Center, Moroccan Foundation for Advanced Science Innovation and Research (MAScIR), Rabat, Morocco; **Khalil Aouadi**, Mohammed ElJazouli, Rabat Design Center, Moroccan Foundation for Advanced Science Innovation and Research (MAScIR), Rabat, Morocco; and Applied Mechanics and Systems Research Laboratory (LR03ES06), Tunisia Polytechnic School, University of Carthage, B.P. 743, 2078 La Marsa, Tunisia; **Meriem Ben Ali**, **Abdelouahed Chbihi**, and **Sanae Naamane**, Mohammed ElJazouli, Rabat Design Center, Moroccan Foundation for Advanced Science Innovation and Research (MAScIR), Rabat, Morocco; **Nawal Semlal**, OCP Group S.A., 2-4, Rue Al Abtal-Hay Erraha, 20200 Casablanca, Morocco; **Hassan Bouaouine**, Mohammedia School of Engineers (EMI), Mohammed V University, Avenue Ibn Sina, B.P. 765, Agdal, Rabat, Morocco. Contact e-mail: a.eljersifi@mascir.ma.

Chemical composition affects the properties of HCCIs through the nature of their carbides and the type of their matrix. Carbides come in different stoichiometries and crystallographic structures. The three main types frequently found in the Fe-C-Cr system are the  $M_3C$ ,  $M_7C_3$  and  $M_{23}C_6$  variants. Depending on the chemical composition of the alloy, and in particular, its chromium content, some carbides are more stable than others. Actually, below 12% in chromium mass percentage, the  $M_3C$  carbides form is dominant. They are characterized by their lower hardness and limiting effect on the alloy's toughness (Ref 6, 7), whereas for higher percentage values, the  $M_7C_3$  form is dominating. This form is characterized by its discontinuity, compared to the  $M_3C$  carbides, and their higher hardness that varies between 1400 and 1600 HV (Ref 6). For even higher chromium content, and lower carbon contents, the  $M_{23}C_6$  form is more likely to be obtained (Ref 7, 8). However, it is hard to predict exactly at which exact chromium and carbon mass percentages the form changes. Considering its importance in the industry, extensive research works have been led in order to better understand the Fe-C-Cr systems and determine how the  $M_{23}C_6$  field extends from the binary Cr-C edge. There is, however, no consensus in this regard among all authors (Ref 9-11).

In general, the higher the carbide volume fraction (CVF) is the better wear resistance (Ref 1). However, this is not the case when higher carbon contents lead to carbides that are coarser, harder and tougher (Ref 2, 12) but prone to spalling (Ref 1, 2) which reduces the alloy's overall wear resistance. These alloys also suffer from high reject rate and brittleness which limit their use (Ref 2), although some tougher hypereutectic HCCIs have been developed (Ref 13).

Moreover, chemical composition affects the nature of the alloy's matrix. Most commercially available high-chromium cast irons are austenitic by nature due to the high content in carbon, which stabilizes austenite (Ref 14, 15). To further improve hardness and wear resistance, a martensitic matrix is preferable. In most cases, a partial transformation from

austenite to martensite can happen without any treatment. This is because austenite is metastable and can only remain in the matrix at room temperature if the alloying content is high enough (Ref 1, 16, 17). In some cases, undesirable pearlitic formation in the matrix can also happen. This can be avoided by the addition of alloying elements, such as silicon, copper and manganese. However, this implies the rise of the temperature where martensitic transformation begins, called  $M_s$  (martensite start), hindering the martensitic transformation in favor of an over-stabilized austenite. Molybdenum is an exception to that rule and can inhibit pearlite formation without raising the  $M_s$  temperature (Ref 1, 18).

Heat treatments are another method used to improve the properties of high-chromium cast irons. This goal can be achieved through several methods, and the destabilization heat treatments are among the most used. This technique induces the precipitation of secondary carbides inside the matrix which destabilizes austenite in favor of martensite. The reduction of the residual austenite content and the increase martensite content results in the increase in hardness and wear resistance (Ref 1, 19, 20).

In some cases, the presence of some amount of residual austenite in the treated alloy is desirable, such as when impact resistance is a priority (Ref 21, 22). But, when the residual austenite remains undue, the submission of the destabilized sample to a subcritical or a cryogenic heat treatment is known to reduce or even eliminate the austenite content in the matrix (Ref 1). However, the direct application of a subcritical heat treatment on the sample, without a previous destabilization, can lead to a ferritic/pearlitic matrix with significantly lower hardness as observed by Karantzalis et al. on a high-chromium cast iron with 2.35% carbon content and 18.23% chromium content (Ref 19).

In order to reduce the brittleness, improve toughness and release stress, tempering treatment is an appropriate and commonly used heat treatment (Ref 23). Meanwhile, it is worth nothing that such treatment reduces hardness (Ref 20, 23, 24) and might improve wear resistance. Similar results were obtained by Sarac et al. on a HCCI where tempering led to an increase in the number of secondary carbides and a more uniform distribution inside the matrix. Thus, the treatment was more effective in the protection of the matrix during wear testing (Ref 23). It also improved the corrosion resistance through the modification of the shape of primary carbides which made them act as a physical barrier to pitting (Ref 23).

Cooling rates are another heat treatment parameter that can impact the nature of the matrix and carbides. Rivlin et al. (Ref 9) stated that  $M_7C_3$  carbides form, instead of their  $M_{23}C_6$  counterparts, if the cooling rate is high enough. The same behavior was observed by Wiczerzak et al. (Ref 8) while studying a high-chromium cast iron with 0.8% carbon content and 24.5% chromium content. For the matrix, slow cooling rates lead to the formation of a pearlitic matrix with lower hardness (Ref 1), while faster cooling rates affect martensitic transformation of the matrix as well, as described by Tupaj et al. (Ref 25) in their study of a 15% Cr high-chromium cast iron where a higher cooling rate reduced  $M_s$  temperatures.

At high Cr/C ratios, high-chromium cast irons form a ferritic matrix. This can be undesirable as ferrite is softer than martensite and does not experience work-induced hardening when exposed to wear as austenite does (Ref 26, 27). However,

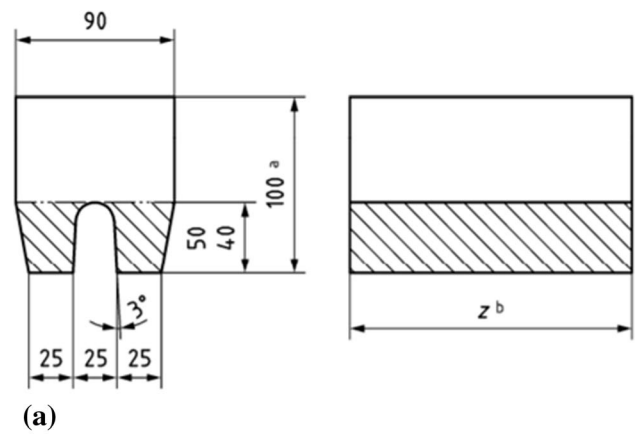


**Fig. 1** The shape of the cast bloc of high-chromium cast iron before cutting and machining: (a) schematic from the DIN 1563:2012-03 standard where the cross-hatched zone is the one to be extracted for sample extraction. (b) A cast bloc before machining

**Table 1** Chemical composition of the high-chromium cast iron

Element	C	Cr	Ni	Mo	Si	Mn
Mass percentage	1.1	29.27	0.2	1.1	1.18	0.64

higher chromium content in the matrix makes those alloys more resistant to corrosion than the other HCCIs (Ref 27). These alloys are used in environments where wear resistance is less of a threat than corrosion. Yet, there are only few researches related to ferritic high-chromium cast irons since they are considered “un-heat treatable” (Ref 27) and rarely experience any phase transformation due to heat treatment.

In this work, we explored the effects of heat treatments on such alloys, by subjecting a ferritic high-chromium cast iron to several heat treatments. These heat treatments are similar to the destabilizing heat treatments commonly used in the industry on their austenitic counterparts. Samples’ resistance to erosion and corrosion is studied, as well as their hardness and microstructural changes.

## 2. Materials and Methods

The objective of this study is to examine the effects of heat treatments on the properties and microstructure of a ferritic high-chromium cast iron. For that purpose, samples were subjected to hardness testing, metallographic analysis, corrosion testing and erosion jet impingement testing, post-treatment.

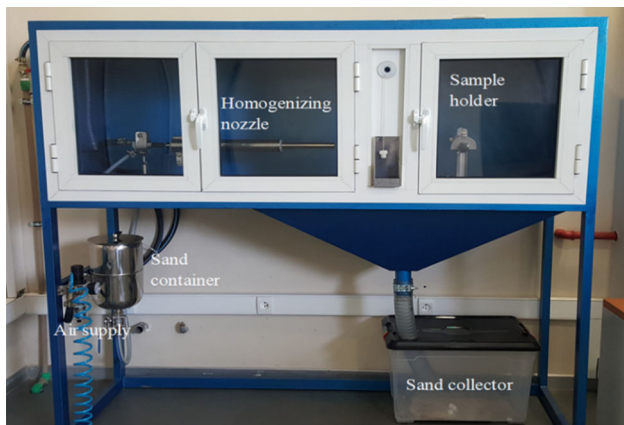


Fig. 2 Jet impingement erosion tester used in this study

### 2.1 Sample Preparation

First, a U-shaped bloc was cast into dry sand molds according to the DIN 1563:2012-03 standard which specifies the shape and dimensions of cast samples destined for mechanical testing. The dimensions and shape of the casting are shown in Fig. 1; in this case the chosen Z value was 240 mm. The obtained bloc was then cut using a mechanical saw at first, afterward using a Struers Labotom-5 tabletop cutting machine for smaller sized samples. Water lubrication was used so as to avoid any heat-related effect on the samples' properties during the two cutting steps. The dimensions of each sample were  $30 \times 36 \times 5$  mm.

A sample was used for the determination of the chemical composition using an SEOS2 spark emission optic spectrometer. Five iterations of the test were done, and the average values of the mass percentages are summarized in Table 1.

Heat treatments were applied using a Thermolyne 48,000 furnace. Four holding temperatures were chosen for this study, starting from 800 °C, with 100 °C increments. The furnace was heated up to the targeted temperatures, and the samples were introduced for 2 h and then subsequently air-cooled. The procedure was repeated for each temperature. At 1100 °C, two samples were tested, one of which was cooled using compressed air, to investigate the effect of cooling rate on the sample's properties.

Samples were carefully polished using multiple SiC emery papers up to 1200-grit. They were then polished using three solutions containing diamond particles in suspension with sizes

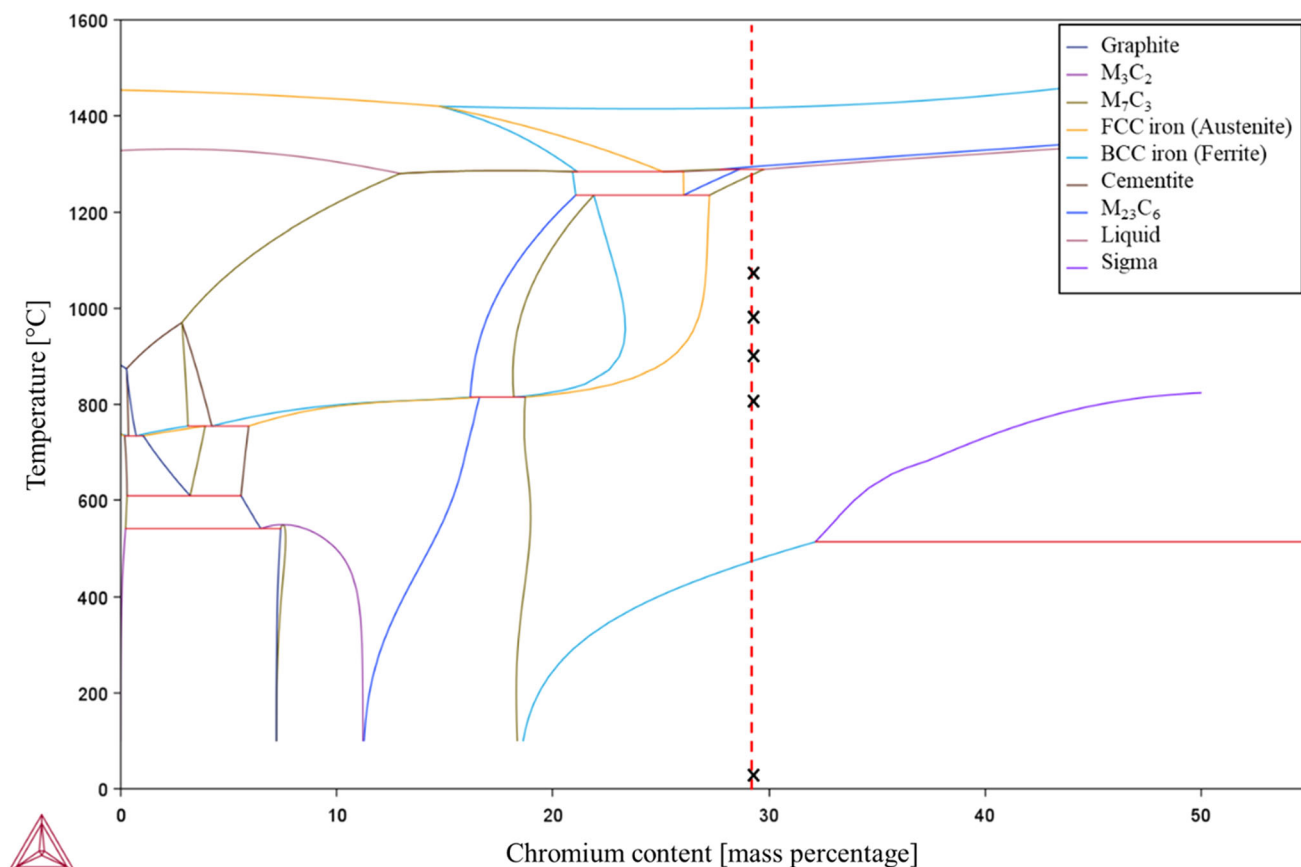


Fig. 3 Equilibrium phase diagram of the high-chromium cast iron for the specified chemical composition. The “x” shows the samples' position on the diagram

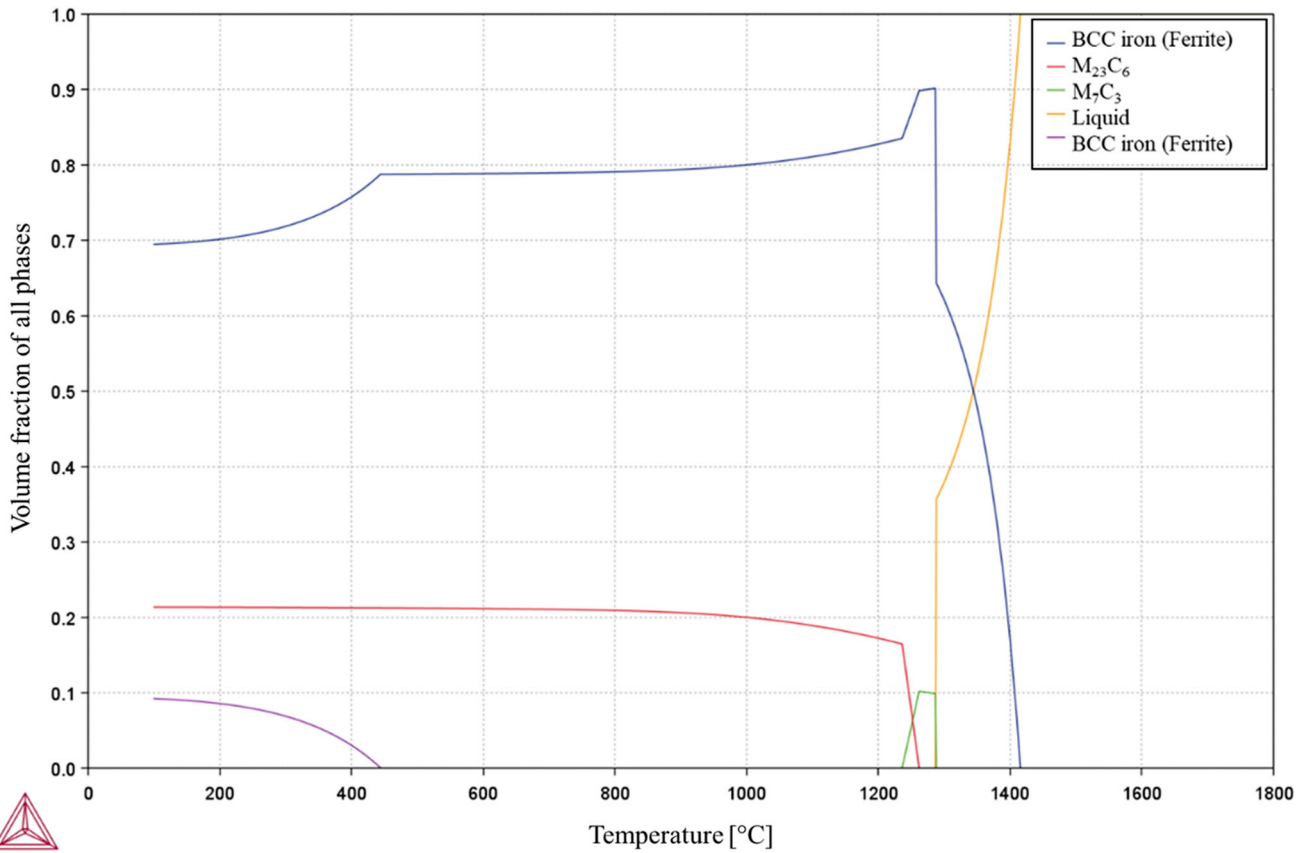


Fig. 4 Variation of phase fraction versus temperature of the sample

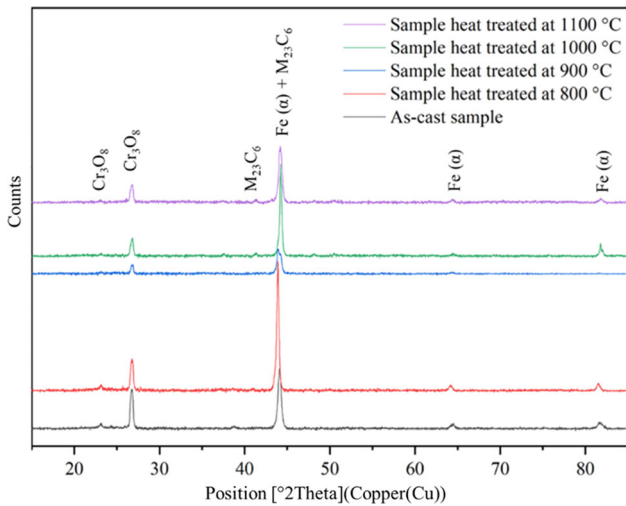


Fig. 5 Multiple x-ray diffractograms of the as-cast and heat-treated samples identified:  $\text{Cr}_3\text{O}_8$  chromium oxide,  $\text{M}_{23}\text{C}_6$  chromium carbides and alpha ferrite

of 6, 3 and  $1\ \mu\text{m}$ , respectively. A set of 6 samples per heat treatment was prepared for a full characterization.

## 2.2 Characterization Methods

**2.2.1 Hardness and Microhardness Testing.** For hardness testing, 4 samples representing each heat treatment were tested, in addition to the as-cast state. For each sample, twenty

HV10 indentations were made to evaluate their mean hardness. An AFRI WIKI 90JS hardness tester with a Vickers indenter was used, according to the ISO6506 standard. As no etching was necessary to differentiate the carbides from the matrix, the microhardness indentations were directly made into the sample. For each phase, twenty indentations were made: HV0.01 indentations on the carbides and HV0.05 indentations on the matrix. The indentation's load was chosen so as to maximize its size, which reduced the error rate, while keeping it inside the phase. In both cases, a 15 s dwell time followed indentation. Care was taken to exceed a minimum distance between indentations that was equal to 2.5 times the diameter of those indentation.

**2.2.2 Corrosion Testing.** A BioLogic SP-50 potentiostat, with an Ag/AgCl reference electrode and a platinum wire counter-electrode, was used to evaluate the corrosion resistance of the samples. Samples were cut into a smaller surface of  $1\ \text{cm}^2$ . A copper wire was then attached to one side of each one, covered using copper tape and then embedded in resin. This was done in order to expose only one surface of the sample while ensuring an electrical connection with the potentiostat.

The samples were then polished following the same procedure as detailed above. As it is possible for user error to deviate the samples' surface from the intended  $1\ \text{cm}^2$  value, measurements were made and noted so that they could be considered when the polarization curves are drawn.

Sulfuric acid was chosen as a corrosive agent since it is commonly used in applications where high-chromium cast irons are used. Examples of these applications include the use

**Table 2 Mean contents in the three major elements of the alloy (iron, carbon and chromium) in the matrix and carbides for all samples as found from the EDX analysis**

		C	Cr	Fe	M-to-C ratio in carbides
As-cast	Matrix	0	24.74	71.14	4.18205945
	Carbides	21.175	59.355	16.705	
Heat treated at 800 °C	Matrix	0	24.67	71.12	3.03206203
	Carbides	24.71	55.372	18.148	
Heat treated at 900 °C	Matrix	0	22.38	71.08	4.5759201
	Carbides	15.343	65.436	17.726	
Heat treated at 1000 °C	Matrix	0	20.77	75.43	4.63254884
	Carbides	15.203	64.496	18.79	
Heat treated at 1100 °C	Matrix	0	22.39	73.1278	6.0463223
	Carbides	12.36875	57.3525	28.24	

of sulfuric acid for chemical leaching to obtain metals such as iron (Ref 28, 29) and copper (Ref 30) which generates erosive particles, and the wet process acid (WPA) of phosphoric acid production which generates phosphogypsum particles. These particles are highly erosive for the exposed components. Thus, the chosen alloys to build those components must resist to both erosion and corrosion.

A 1.5L solution of 0.5 M H<sub>2</sub>SO<sub>4</sub> at room temperature was prepared, and 50 to 100 ml of the portions was used for each test. This method was used in order to prevent the contamination of the solution during tests and to make sure that the same exact acid concentration was used for each test.

Open corrosion potential measurements (OCP) were undergone for 12 h, at a rate of one measurement per second, or per variation of 1 mV, in a potential range of  $-2.5$  V to 2.5 V, at a resolution of 100  $\mu$ V. Those measurements were followed by polarization testing which varied the applied potential from  $-0.5$  to 1.3 V, with a 20 mV/min scan rate, at the same resolution.

**2.2.3 Dry Erosion Testing.** Erosion testing was performed in order to evaluate the effect of particle impact on the surface of samples, as it was more indicative of their erosion resistance than just hardness testing. To that purpose, a jet impingement erosion tester, capable of ejecting particles at high velocities using compressed air, was used (Fig. 2). More details about the operation mode and calibration process are described by Matal et al. (Ref 31). Samples were maintained at 80 cm distance from the nozzle and exposed to a jet of SiC particles at 25 m.s<sup>-1</sup>. Particle sizes ranged between 500 and 710  $\mu$ m. Samples were held at an impingement angle of 5°.

To measure mass loss, samples were weighed before and after each test using an OHAUS PA214 electronic balance with a display accuracy 0.1 mg. Erosion rates were defined as the ratio of mass loss to test duration in mg.s<sup>-1</sup>. Maximum standard error of the mean was found at 0.00115.

**2.2.4 Metallographic Analysis.** To reveal the samples' microstructure, etching was done post-polishing. Several etching solutions were tested and solution 89 from the ASTM 407-99 standard was found to be the most effective. The solution consists of 10 ml of nitric acid, 10 ml of acetic acid, 15 ml of hydrochloric acid and 2 to 5 drops of glycerol. Each

sample was soaked for 20 to 60 s in the mixture, then cleaned using de-ionized water followed by acetone and let to air dry. Samples were then examined using a Zeiss AXIO Vert A1 inverted optical microscope. For this study, the phase analysis module of the ClaraVision software was used to calculate the carbide volume fraction (CVF). The surface fraction of the carbides per micrograph is averaged over a minimum of 15 images per sample, at a 200 $\times$  magnification.

To quantify the change in carbide morphology observed post-heat treatment, mean carbide thickness was also determined. As carbides adopt elongated forms, it was easy to determine their individual thickness by measuring the width, from edge to edge, of the carbide at its approximate center. This was done on all found on the same micrographs used for CVF calculations. The mean value over all micrographs was determined for each sample.

Ferrite grain size was determined using method B of the ISO 13383-1:2012 standard, as opposed to using one of the intercept methods commonly used for grain size determination. This alternative method was chosen to overcome the difficulty encountered with heterogeneous alloy and carbides. This method called "the mean equivalent circle diameter method" is based on the identification of the circle which best estimates the grain limits.

The samples were also analyzed using a FEI Tecnai G2 120 kV SEM-EDX operating at an accelerating voltage of 20.0 kV, at high vacuum, for a working distance of 10 mm and a spot size of 3. The analysis mainly examined the microstructure and the chemical composition variation in different phases from one sample to the other.

The samples were finally deep-etched by putting them in an ethanol solution with 10% HCl for 24 h to further examine the chromium carbides. The samples were then cleaned using acetone and air-dried before being examined by scanning electronic microscopy (SEM).

Another set of samples was separately prepared, without etching, for x-ray diffraction (XRD) analysis to confirm the phase composition. The analysis was realized using a Bruker D2-Phaser XRD diffractometer using a Cu K $\alpha$  x-ray source, with 2 $\theta$  in the range 20-80 for a resolution of 0.02° per step for a total test time of 2 h 3 min and 36 s. Phases were identified using the ICDD Pdf-2 database.

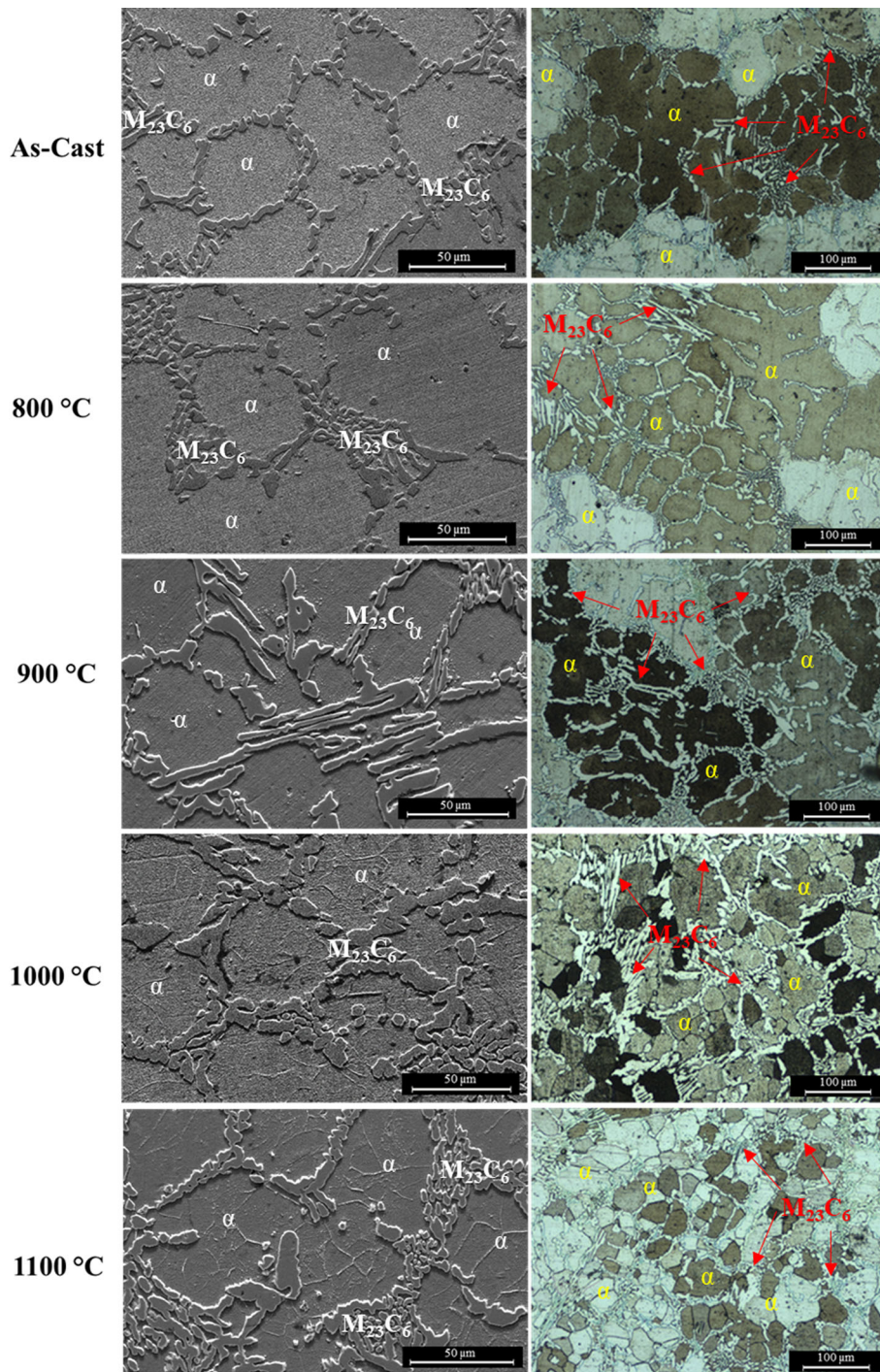


**Fig. 6** Microstructural evolution of the ferritic high-chromium cast iron analyzed using: (a) SEM at a 1000X magnification using an SE detector, (b) optical microscopy at a 200X magnification

### 3. Results and Discussion

#### 3.1 Microstructure

Prior to this analysis, a phase diagram was predicted based on the alloy's chemical composition, using ThermoCalc's Calphad tool (Fig. 3). The simulation points to a dual microstructure composed of ferrite and  $M_{23}C_6$  chromium carbides. Using the same software, the variation of phase fractions depending on the temperature was also determined,

and no phase transformation was detected for the applied heat treatments (Fig. 4).

An XRD analysis was performed on the as-cast and heat-treated samples. The diagrams shown in Fig. 5 confirm the presence of the predicted phases. They also confirmed that no phase transformation was obtained after the heat treatments. The variations in peak positions due to thermal strain were insignificant.

Since XRD peaks are similar for the  $M_{23}C_6$  and  $M_7C_3$  carbides, it was important to further investigate the nature of the

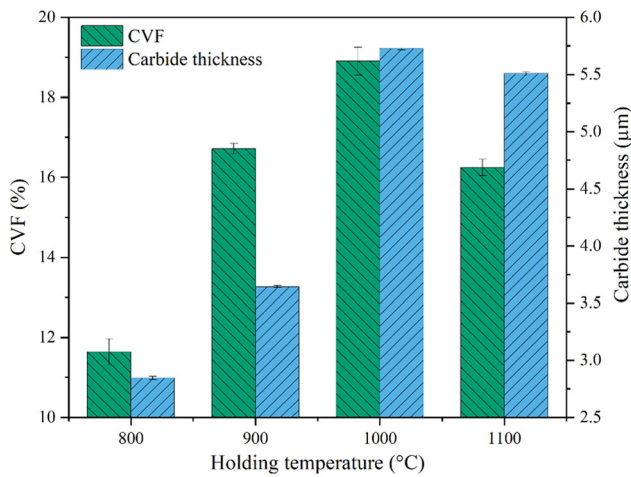


**Fig. 7** Carbide volume fraction (CVF) and carbide thickness evolution versus the holding temperature of the sample

chromium carbides. In this order, all samples were subject to an EDX analysis. The obtained results confirmed that their stoichiometry was closer to the  $M_{23}C_6$  variant, where the M-to-C ratio is about 3.833, than to the  $M_7C_3$ 's, where the ratio is around 2.33. The mean chromium, iron and carbon contents found from the EDX analysis, both in the matrix and carbides, are given in Table 2.

Figure 6 shows the microstructural images taken using the SEM at a 1000X magnification, using the secondary electrons (SE) detector (left), along with the ones taken using optical microscopy at a lower magnification of 200X (right). No significant changes were noticed between the as-cast sample and the one that was heat treated at 800 °C. Both samples exhibited a heterogeneous microstructure made of a discontinuous network of chromium carbides in a ferrite matrix. The ferritic nature of the matrix was expected due to the high amount of chromium, a ferrite stabilizer (Ref 32, 33) and a lower amount of carbon, an austenite stabilizer (Ref 14, 33). At 900 °C, carbides grow larger and thicker than their predecessors. This trend is more apparent at 1000 °C where the carbides

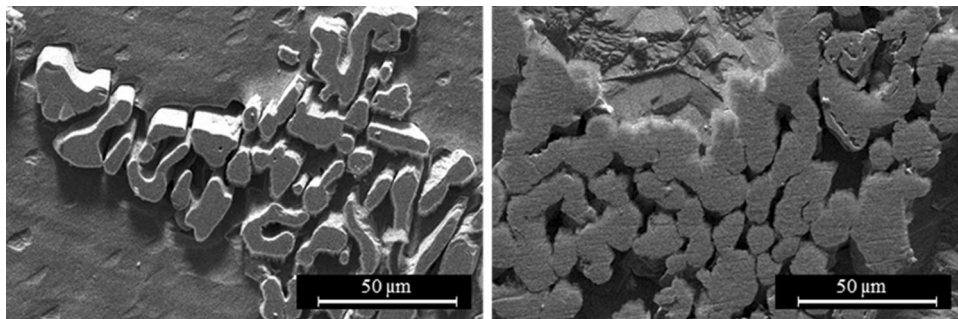


**Fig. 8** SEM images taken using the SE detector at 3000 × magnification of the deep-etched samples showing chromium carbides from the as-cast sample in their normal state (left) and after experiencing coalescence at 1000 °C (right)

**Table 3** HV10 and HV0.05 mean hardness and microhardness values found in the alloy and its matrix, respectively

Holding temperature, °C	Sample hardness (HV10)	Matrix microhardness (HV0.05)
800	272.2	234.308
900	273.506	251.62
1000	276.925	265.356
1100	291.741	222.18

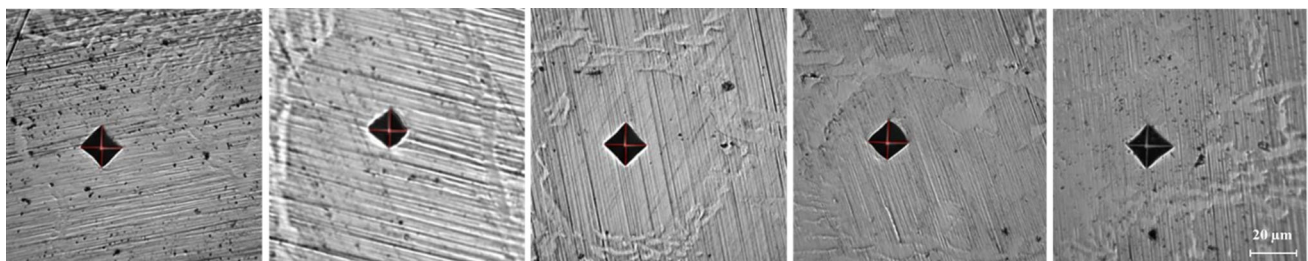


**Fig. 9** Micrographs of the microhardness indentations performed on the matrix at a magnification of 1000X. From left to right: as-cast sample, sample heat treated at 800 °C, sample heat treated at 900 °C, sample heat treated at 1000 °C, sample heat treated at 1100 °C

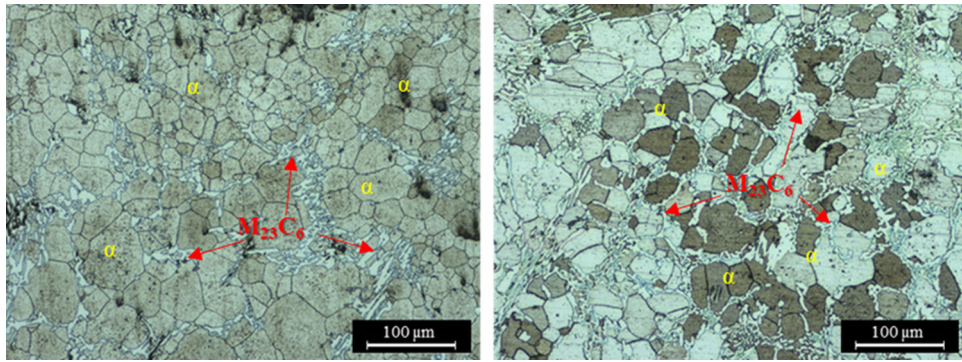


**Fig. 10** Microstructure of 2 heat-treated samples at 1100 °C. Left sample was cooled using compressed air, while the right sample was air-cooled (Magnification: 200X)

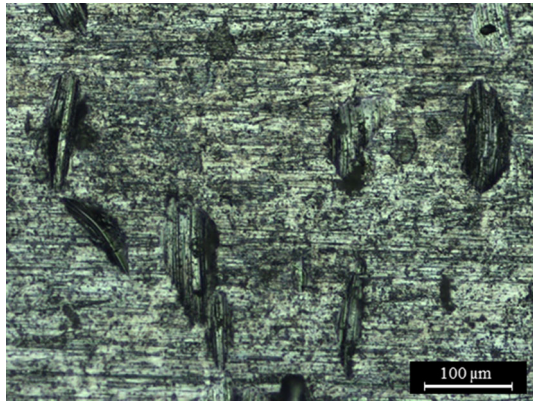


**Fig. 11** Erosion impacts on as-cast samples. (Magnification: 200X)

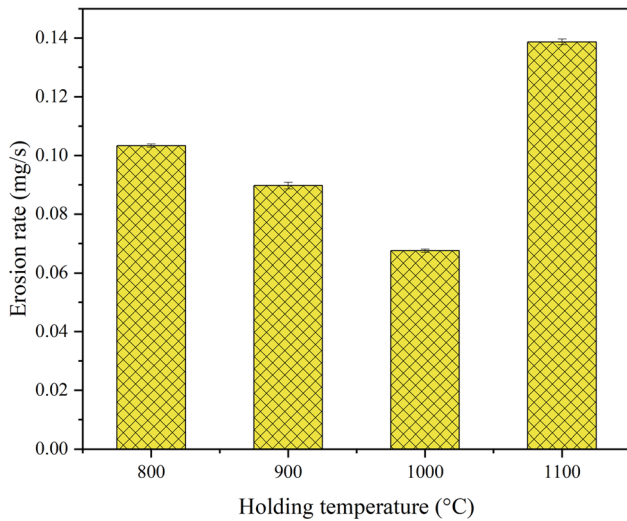


**Fig. 12** Erosion rates of as-cast and heat-treated samples

have rounder edges. In some areas of this sample, partial ferrite recrystallization was observed as can be seen from the corresponding optical micrograph shown in Fig. 6b. Finally, for the sample heat treated at 1100 °C, the size of the carbides starts to slightly decrease compared to the two previous samples, and ferrite recrystallization can be observed in the majority of the sample.

Aside from ferrite recrystallization, two other phenomena were induced by the heat treatment: carbide coalescence and carbide partial dissolution.

Indeed, carbide coalescence started at 900 °C where smaller carbides combined to form larger ones. The process was more noticeable at higher temperatures where this diffusion-controlled process was further accelerated (Ref 8). This mechanism affected both the carbide volume fraction and the mean carbide thickness (Fig. 7) as it raised both up until 1000 °C. The SEM images of deep-etched samples show further the coalescence process (Fig. 8). Beyond that temperature, carbides started experiencing partial dissolution which lowered both their volume fraction and mean thickness.

### 3.2 Hardness and Microhardness

Results of the hardness and the matrix's microhardness tests are given in Table 3. No significant variation was observed for the carbides' microhardness. Their microhardness values varied between 1300 and 1800 HV.

The as-cast sample reaches a mean HV10 hardness value of 253. This value slightly increases when heat treatments were applied and keep rising with increasing temperature. At 1100 °C, the highest value 291.7 HV is reached.

In all samples but the last, hardness values are dictated by the CVF. This is because the hardness of high-chromium cast irons is highly dependent on the volume fraction. This was expected as carbides constitute a high-chromium cast iron hard phase and the main contributor in hardness and wear resistance (Ref 1, 4). This explains the steady increase in the hardness of samples, as the CVF steadily increases in a similar tendency.

At 1100 °C, although CVF drops, the overall hardness rises to reach its maximum value. This might be due to the recrystallization phenomena which leads to the formation of small ferrite grains inside the matrix. The newly formed grain boundaries acted as a barrier to dislocation movement leading to higher hardness value overall as stipulated by the Hall–Petch law (Ref 34, 35). At that same temperature, we notice that contrary to the hardness value of the alloy, matrix microhardness drops. This is because in the case of the HV10 hardness test, the indenter penetrated a larger area that spanned multiple grains, whereas microindentations were limited to fewer or single grains. Inside the grain, recrystallization led to a decrease in dislocation density and their redistribution into more stable configurations energetically (Ref 36), which ultimately reduced their microhardness. Micrographs of the indentations are given in Fig. 9.



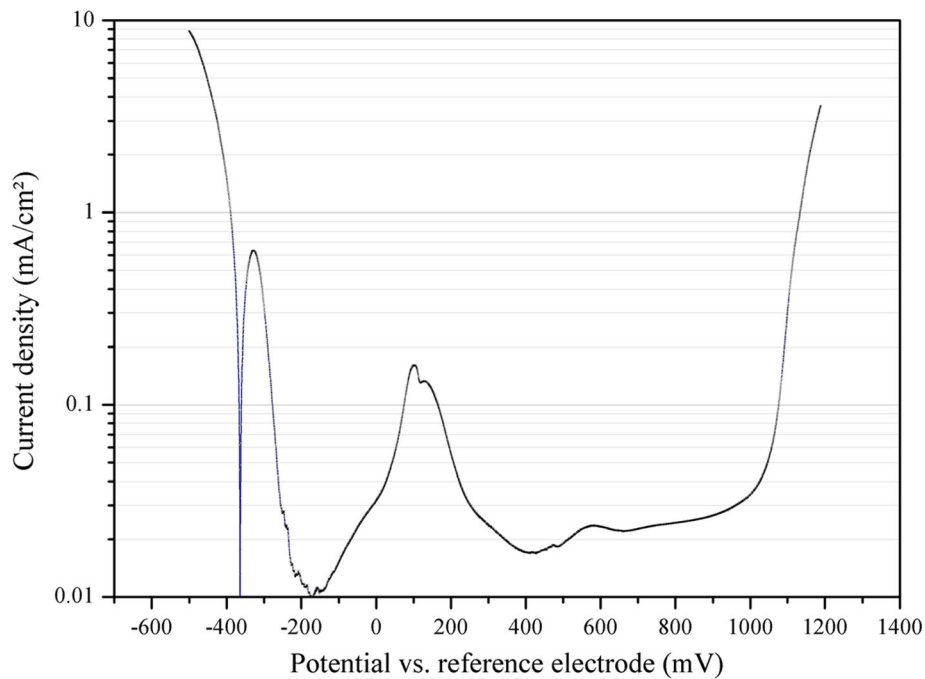


**Fig. 13** Potentiodynamic curve of the as-cast sample

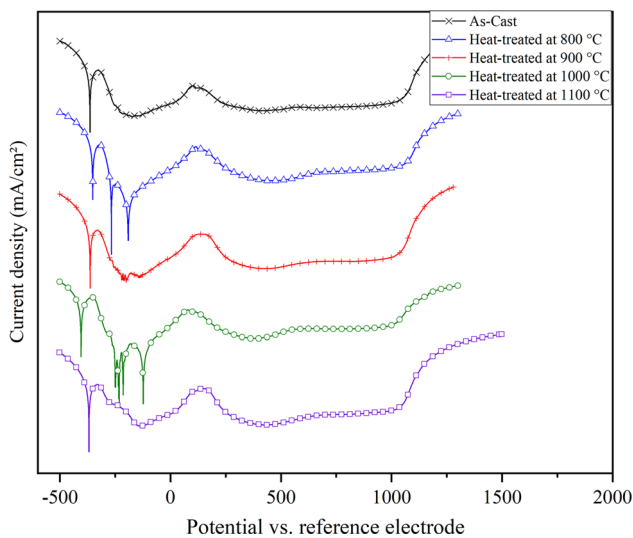


**Fig. 14** Potentiodynamic curves of all samples

To better understand the effect of recrystallization on HV10 hardness, a similar sample was prepared and cooled using compressed air for higher cooling rates. Smaller grain sizes were found at a mean value of  $40.06 \mu\text{m}$  compared to the higher  $43.05 \mu\text{m}$  found for its air-cooled counterpart. A higher hardness of  $305.97 \text{ HV}$ , on the HV10 scale, was determined for this sample although both samples' matrices generated similar single-grain microhardness values. The microstructure of both samples is exhibited in Fig. 10.

### 3.3 Dry Erosion Testing

Under the optical microscope, it can be seen that the erosion impacts adopt an elongated form (Fig. 11). This form is characteristic of the cutting erosion mechanism that happens at

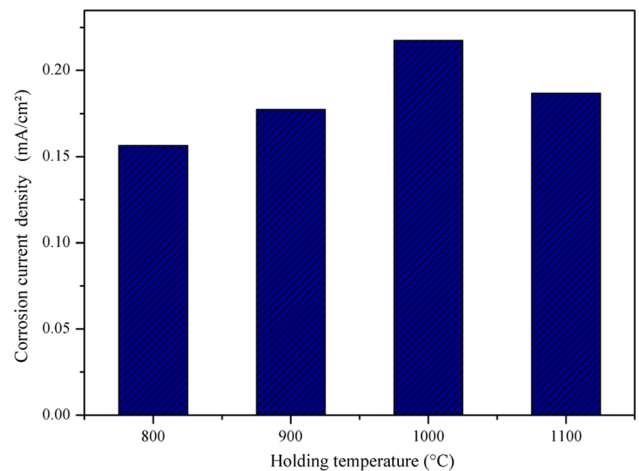


**Fig. 15** Corrosion current densities determined from the potentiodynamic curves for all samples

oblique angles and mostly removes materials without any plastic deformation (Ref 37-39).

Generally, when hardness increases, so does wear resistance (Ref 37, 38). However, as shown in Fig. 12, a higher erosion resistance was registered at  $1000 \text{ }^\circ\text{C}$  which had a lower HV10 hardness value than  $1100 \text{ }^\circ\text{C}$ . At  $1100 \text{ }^\circ\text{C}$ , erosion resistance was at its lowest, with a mass loss value of  $0.1386 \text{ mg}\cdot\text{s}^{-1}$ .

In this case, erosion rate was more dependent on single-grain hardness as the mean impact size was around  $35.31 \mu\text{m}$ . Therefore, it is less affected by the grain boundaries which explains why the erosion rates and the matrix's microhardness values were inversely proportional.

Another factor that affected erosion resistance was the size and the shape of carbides as CVF and carbide thickness both decreased at  $1100 \text{ }^\circ\text{C}$  due to their partial dissolution. Being the

harder phase, they affect the overall wear resistance (Ref 1). Hence, an increase in their volume fraction should lead to a better wear resistance, as it was the case for this alloy.

### 3.4 Corrosion Testing

The corrosion potential of the alloy in its as-cast state was determined to be  $-364.65$  mV. Its current density reached a value of  $0.1561$  mA/cm<sup>2</sup>. Corrosion potential was higher than that obtained by Wiengmoon et al. (Ref 27) in their study involving multiple high-chromium cast irons in the same corrosive solution. According to the same authors (Ref 27), the pearlitic and austenitic variants values are equal to  $-590$  mV and  $-570$  mV, respectively, both lower than the ferritic variant found in our work, highlighting its superior resistance to corrosion in a similar environment.

According to Wiengmoon et al. (Ref 27), corrosion current densities were found to be lower than the  $2.5$  mA/cm<sup>2</sup> of the pearlitic high-chromium cast iron and the  $1.7$  mA/cm<sup>2</sup> of the austenitic one. Those results corroborate the superior performance of our studied alloy in acidic environments which is due to the higher Cr/C ratio (26.6).

The polarization curve is given in Fig. 13. Following the corrosion potential, a first corrosion-resistant oxide layer attempts to form with current density reaching a low value of  $0.012$  mA/cm<sup>2</sup> at  $-174.59$  mV. This layer is quickly broken down, and another current density peak appears marking the final active-passive transition at  $104.89$  mV. The wide transition peak and its double-peak format are due to the superposition of the polarization behaviors of the ferrite matrix and the chromium carbides (Ref 27). Following that transition, passivity settles and stabilizes with current density values reaching  $0.0205$  mA/cm<sup>2</sup>. It is then broken down at  $1001.83$  mV and the material finally enters the transpassivation zone.

When comparing the potentiodynamic curves of all heat-treated samples together (Fig. 14), no significant changes are observed in their overall shape, except for the cathodic loop experienced by most of heat-treated samples. The phenomenon is common to corrosion resistant alloys and is caused by the close values adopted by the cathodic and passive current densities (Ref 40). The polarization curves found for the rest of the samples similarly start with a short-lived oxide layers and followed by an active-passive transition peak adopting the same double-peak format.

When examining electrochemical parameters, no significant variation is found compared to the corrosion potentials. However, an important difference is noticed when comparing corrosion current densities. As shown in Fig. 15, current density values gradually rise, pointing out to higher corrosion rates, and then decrease at  $1100$  °C. The maximum value was obtained at  $1000$  °C with a corrosion current density value of  $0.2174$  mA/cm<sup>2</sup>.

High-chromium cast irons experience commonly called “inter-phase” corrosion and is a form of microgalvanic corrosion caused by the large potential difference between the matrix and the chromium carbides (Ref 41, 42). This form of corrosion starts at the carbide-matrix interface where chromium content is smaller. Being a form of microgalvanic corrosion, the volume fraction of one phase relative to the other affects corrosion current density. This is observed when comparing the variation of CVF and carbide thickness (Fig. 7) to the variation of corrosion current density. This can also be deduced from the effect of deep etching on the samples, as its corrosion damage

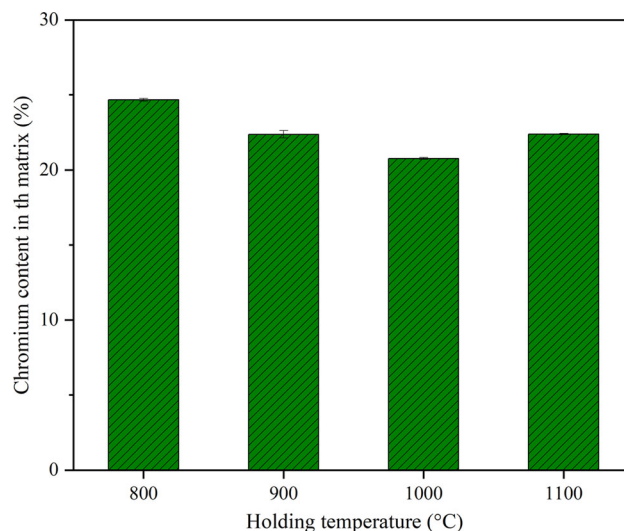


**Fig. 16** Chromium mass percentage in the matrix as measured by EDX analysis

was mainly restricted to the matrix and the carbides were left virtually unaffected (Fig. 8).

Another important factor that impacted corrosion current density is the chromium content in the matrix. At  $1100$  °C, partial carbide dissolution caused an increase in chromium content in the matrix (Fig. 16). As chromium content increases in the matrix, the phase's corrosion resistance increases too (Ref 43), thus reducing potential difference between the matrix and carbides, leading to the alloy's overall better corrosion resistance.

## 4. Conclusion

Ferritic high-chromium cast irons are more resistant to corrosion than their austenitic and martensitic cast iron counterparts. However, their hardness and wear resistance are lower and they are less responsive to heat treatment. Heat treating them can lead to three microstructural phenomena, all of which impacted the alloy's properties one way or another:

- The coalescence of chromium carbides led to larger carbides and slightly increased CVF. This led to higher hardness values as well as better erosion resistance. This phenomena's effect was noticed right up to  $1000$  °C.
- At  $1100$  °C, carbides start to experience partial dissolution. This led to a lower CVF value which reduced in turn erosion resistance. This also increased chromium content in the matrix leading to an overall improvement of the corrosion resistance.
- The third phenomenon was ferrite recrystallization occurring at  $1100$  °C, although it was partially detected at  $1000$  °C in some zones of the sample. This recrystallization led to smaller grain sizes and caused an increase in the overall hardness. However, because of the decrease in dislocation density, single-grain hardness fell, causing a reduction in erosion resistance. No notable relation between ferrite recrystallization and corrosion resistance was elucidated.

The effect of heat treatments on the overall corrosion resistance, hardness and wear resistance varied depending on the heat treatments parameters. When corrosion resistance is more of a threat than wear resistance, going to 1100 °C is the recommended approach, while temperatures below it will have the reverse effect. A careful choice of heat treatment parameters will certainly increase the service life of components.

## Acknowledgments

The authors would like to thank OCP Group S.A. for providing the data used for this study. Thanks are also extended to Dr. Ganetri Ikram for her help in revising the manuscript.

## Funding

This work was financially supported by the OCP foundation, Grant No: MAT-NAA-01-2017, 2018.

## Conflict of interest

The authors declare that they have no known competing financial interests or personal relationships that could have appeared to influence the work reported in this paper.

## References

- C.P. Tabrett, I.R. Sare, and M.R. Ghomashchi, Microstructure-Property Relationships in High Chromium White Iron Alloys, *Int. Mater. Rev.*, 1996, **41**(2), p 59–82.
- R.J. Llewellyn, S.K. Yick, and K.F. Dolman, Scouring Erosion Resistance of Metallic Materials Used in Slurry Pump Service, *Wear*, 2004, **256**, p 592–599. <https://doi.org/10.1016/j.wear.2003.10.002>
- E. Zumelzu, I. Goyos, C. Cabezas, O. Opitz, and A. Parada, Wear and Corrosion Behaviour of High-Chromium (14-30% Cr) Cast Iron Alloys, *J. Mater. Process. Technol.*, 2002, **128**(1–3), p 250–255. [https://doi.org/10.1016/S0924-0136\(02\)00458-2](https://doi.org/10.1016/S0924-0136(02)00458-2)
- Z. Guo, F. Xiao, S. Lu, H. Li, and B. Liao, Effects of Heat-Treatment on the Microstructure and Wear Resistance of a High-Chromium Cast Iron for Rolls, *Adv. Mater. Sci. Eng.*, 2016, **2016**, p 1–8.
- M.A. Al-bukhaiti, S.M. Ahmed, F.M.F. Badran, and K.M. Emara, Effect of Impingement Angle on Slurry Erosion Behaviour and Mechanisms of 1017 Steel and High-Chromium White Cast Iron, *Wear*, 2007, **262**, p 1187–1198. <https://doi.org/10.1016/j.wear.2006.11.018>
- A. Wiengmoon, Carbides in High Chromium Cast Irons, *Naresuan Univ. Eng. J.*, 2011, **6**(1), p 64–71.
- G.L.F. Powell and G. Laird, Structure, Nucleation, Growth and Morphology of Secondary Carbides in High Chromium and Cr-Ni White Cast Irons, *J. Mater. Sci.*, 1992, **27**(1), p 29–35. <https://doi.org/10.1007/bf00553833>
- K. Wiczerzak et al., The Effect of Temperature on the Evolution of Eutectic Carbides and M7C3 → M23C6carbides Reaction in the Rapidly Solidified Fe-Cr-C Alloy, *J. Alloys Compd.*, 2017, **698**, p 673–684. <https://doi.org/10.1016/j.jallcom.2016.12.252>
- V.G. Rivlin, 14: Critical Review of Constitution of Carbon-Chromium-Iron and Carbon-Iron-Manganese Systems, *Int. Met. Rev.*, 1984, **29**(1), p 299–327. <https://doi.org/10.1179/imtr.1984.29.1.299>
- W.R. Thorpe and B. Chicco, The Fe-rich Corner of the Metastable C-Cr-Fe Liquidus Surface, *Metall. Trans. A*, 1985, **16**(9), p 1541–1549. <https://doi.org/10.1007/BF02663011>
- A.V. Khvan, B. Hallstedt, and C. Broeckmann, A Thermodynamic Evaluation of the Fe-Cr-C System, *Calphad Comput. Coupling Phase Diagrams Thermochem.*, 2014, **46**, p 24–33. <https://doi.org/10.1016/j.calphad.2014.01.002>
- Ö.N. Doğan, J.A. Hawk, and G. Laird, Solidification Structure and Abrasion Resistance of High Chromium White Irons, *Metall. Mater. Trans. A*, 1997, **28**(6), p 1315–1328. <https://doi.org/10.1007/s11661-997-0267-3>
- G.L.F. Powell, I.H. Brown, and G.D. Nelson, Tough Hypereutectic High Chromium White Iron-A Double In Situ Fibrous Composite, *Adv. Mater. Res.*, 2008, **32**, p 111–114. <https://doi.org/10.4028/www.scientific.net/amr.32.111>
- M. Hernández-Mayoral and M.J. Caturla, Microstructure evolution of irradiated structural materials in nuclear power plants. in *Understanding and Mitigating Ageing in Nuclear Power Plants: Materials and Operational Aspects of Plant Life Management (PLIM)*, Woodhead Publishing Limited, 2010, pp. 189–235
- S.H. Ryu, M.S Kim, Y.S. Lee, J.T. Kim, J. Yu, and B.J. Lee. The effects of carbon and austenite stabilizing elements (Co, Cu, Ni and Mn) on the microstructural changes and the creep rupture strength in 9-12% Cr ferritic heat resistant steels. In *4th International Conference on Advances in Materials Technology for Fossil Power Plants* (Vol. 2005, pp. 1280-1298)
- M.A. Guitar et al., High Chromium Cast Irons: Destabilized-Subcritical Secondary Carbide Precipitation and Its Effect on Hardness and Wear Properties, *J. Mater. Eng. Perform.*, 2018, **27**(8), p 3877–3885. <https://doi.org/10.1007/s11665-018-3347-1>
- T. Sun, R.B. Song, X.U. Wang, P. Deng, and C.J. Wu, Abrasive Wear Behavior and Mechanism of High Chromium Cast Iron, *J. Iron Steel Res. Int.*, 2015, **22**(1), p 84–90. [https://doi.org/10.1016/S1006-706X\(15\)60014-0](https://doi.org/10.1016/S1006-706X(15)60014-0)
- E. Karantzalis, A. Lekatou, and H. Mavros, Microstructure and Properties of High Chromium Cast Irons: Effect of Heat Treatments and Alloying Additions, *Int. J. Cast Met. Res.*, 2009, **22**(6), p 448–456. <https://doi.org/10.1179/174313309x436637>
- A.E. Karantzalis, A. Lekatou, and H. Mavros, Microstructural Modifications of As-Cast High-Chromium White Iron by Heat Treatment, *J. Mater. Eng. Perform.*, 2009, **18**(2), p 174–181. <https://doi.org/10.1007/s11665-008-9285-6>
- D. Kopycinski, E. Guzik, D. Siekaniec, and A. Szczesny, Analysis of the High Chromium Cast Iron Microstructure After the Heat Treatment, *Arch. Foundry Eng.*, 2014, **14**(3), p 43–46. <https://doi.org/10.2478/afe-2014-0059>
- S. Turenne, J. Lavallée, and J. Masounave, Matrix Microstructure Effect on the Abrasion wear Resistance of High-Chromium white Cast Iron, *J. Mater. Sci.*, 1989, **24**, p 3021–3028.
- R. Qichang, H. Beiling, and Z. Qingde, A Study of the Impact Fatigue Resistance of Grinding Balls-Matrices and Retained Austenite, *Wear*, 1991, **151**(1), p 13–21. [https://doi.org/10.1016/0043-1648\(91\)90342-R](https://doi.org/10.1016/0043-1648(91)90342-R)
- M.F. Sarac and B. Dikici, Effect of Heat Treatment on Wear and Corrosion Behavior of High Chromium White Cast Iron, *Mater. Test.*, 2019, **61**(7), p 659–666. <https://doi.org/10.3139/120.111382>
- M. Gelfi, A. Pola, L. Girelli, A. Zacco, M. Masotti, and G.M. La Vecchia, Effect of Heat Treatment on Microstructure and Erosion Resistance of White Cast Irons for Slurry Pumping Applications, *Wear*, 2019, **428**, p 438–448. <https://doi.org/10.1016/j.wear.2019.03.011>
- M. Tupaj, A.W. Orłowicz, A. Trytek, M. Mróz, G. Wnuk, and A.J. Dolata, The Effect of Cooling Conditions on Martensite transformation Temperature and Hardness of 15% cr Chromium Cast Iron, *Materials (Basel)*, 2020, **13**(12), p 1–13. <https://doi.org/10.3390/ma13122760>
- J.T.H. Pearce, The Use of Transmission Electron Microscopy to Study the Effects of Abrasive Wear on the Matrix Structure of a High Chromium Cast Iron, *Wear*, 1983, **89**(3), p 333–344. [https://doi.org/10.1016/0043-1648\(83\)90154-0](https://doi.org/10.1016/0043-1648(83)90154-0)
- A. Wiengmoon, J.T.H. Pearce, and T. Chairuangri, Relationship Between Microstructure, Hardness and Corrosion Resistance in 20 wt.%Cr, 27 wt.%Cr and 36 wt.%Cr High Chromium Cast Irons, *Mater. Chem. Phys.*, 2011, **125**(3), p 739–748. <https://doi.org/10.1016/j.materchemphys.2010.09.064>
- D. El Bar and D. Barket, The Leaching of Sulfide Iron (II) with Sulfuric Acid, *J. Min. Sci.*, 2015, **51**(1), p 179–185. <https://doi.org/10.1134/S106273911501024X>
- L. Tao, L. Wang, K. Yang, X. Wang, L. Chen, and P. Ning, Leaching of Iron from Copper Tailings by Sulfuric Acid: Behavior, Kinetics and Mechanism, *RSC Adv.*, 2021, **11**(10), p 5741–5752. <https://doi.org/10.1039/d0ra08865j>
- M.K. Khalid, J. Hamuyuni, V. Agarwal, J. Pihlasalo, M. Haapalainen, and M. Lundström, Sulfuric Acid Leaching for Capturing Value from Copper Rich Converter Slag, *J. Clean. Prod.*, 2019, **215**, p 1005–1013. <https://doi.org/10.1016/j.jclepro.2019.01.083>

31. A. Matal, M. Karim, and S. Naamane, Development and Calibration of an Experimental Test Bench Simulating Solar Reflectors Erosion, *Sol. Energy*, 2020, **201**, p 724–731. <https://doi.org/10.1016/j.solener.2020.03.028>
32. H. Liou, Y. Pan, R. Hsieh, and W. Tsai, Effects of Alloying Elements on the Mechanical Properties and Corrosion Behaviors of 2205 Duplex Stainless Steels, *J. Mater. Eng. Perform.*, 2001, **10**(April), p 231–241.
33. S. Zhang, Q. Wang, R. Yang, and C. Dong, Composition Equivalents of Stainless Steels Understood Via Gamma Stabilizing Efficiency, *Sci. Rep.*, 2021, **11**(1), p 5423. <https://doi.org/10.1038/s41598-021-84917-z>
34. E.O. Hall, The Deformation and Ageing of Mild Steel: III Discussion of Results, *Proc. Phys. Soc. Sect. B*, 1951, **64**(9), p 747.
35. N.J. Petch, The Cleavage Strength of Polycrystals, *J. Iron Steel Inst.*, 1953, **174**, p 24–28.
36. K.K. Alaneme and E.A. Okotete, Recrystallization Mechanisms and Microstructure Development in Emerging Metallic Materials: A Review, *J. Sci. Adv. Mater. Devices*, 2019, **4**(1), p 19–33. <https://doi.org/10.1016/j.jsamd.2018.12.007>
37. I. Hutchings and P. Shipway, *Tribology: Friction and Wear of Engineering Materials*, Butterworth-Heinemann, Oxford, 2017
38. V. Javaheri, D. Porter, and V.T. Kuokkala, Slurry Erosion of Steel-Review of Tests, Mechanisms and Materials, *Wear*, 2018, **408**, p 248–273. <https://doi.org/10.1016/j.wear.2018.05.010>
39. I. Finnie, Some reflections on the past and future of erosion, *Wear*, 1995, **186**, p 1–10. [https://doi.org/10.1016/0043-1648\(95\)07188-1](https://doi.org/10.1016/0043-1648(95)07188-1)
40. R.G. Kelly, J.R. Scully, D. Shoesmith, and R.G. Buchheit, *Electrochemical Techniques in Corrosion Science and Engineering*, CRC Press, Boca Raton, 2002
41. K.A. El-Aziz, D. Saber, and H.E.D.M. Sallam, Wear and Corrosion Behavior of Al-Si Matrix Composite Reinforced with Alumina, *J. Bio Tribo-Corros.*, 2015, **1**(1), p 1–10. <https://doi.org/10.1007/s40735-015-0026-8>
42. A. Neville, F. Reza, S. Chiovelli, and T. Revega, Characterization and Corrosion Behavior of High-Chromium White Cast Irons, *Metall. Mater. Trans. A*, 2006, **37**(8), p 2339–2347. <https://doi.org/10.1007/BF02586208>
43. B. Sun, X. Zuo, X. Cheng, and X. Li, The Role of Chromium Content in the Long-Term Atmospheric Corrosion Process, *npj Mater. Degrad.*, 2020, **4**(1), p 1–9. <https://doi.org/10.1038/s41529-020-00142-5>

**Publisher's Note** Springer Nature remains neutral with regard to jurisdictional claims in published maps and institutional affiliations.

Springer Nature or its licensor (e.g. a society or other partner) holds exclusive rights to this article under a publishing agreement with the author(s) or other rightsholder(s); author self-archiving of the accepted manuscript version of this article is solely governed by the terms of such publishing agreement and applicable law.